

Extended Thermodynamic Approach for Non-Equilibrium Gas Flow

G. H. Tang^{1,*}, G. X. Zhai¹, W. Q. Tao¹, X. J. Gu² and D. R. Emerson²

¹ MOE Key Laboratory of Thermo-Fluid Science and Engineering, School of Energy and Power Engineering, Xi'an Jiaotong University, Xi'an 710049, P.R. China.

² Computational Science and Engineering Department, STFC Daresbury Laboratory, Warrington WA4 4AD, UK.

Received 30 October 2011; Accepted (in revised version) 18 May 2012

Communicated by Kun Xu

Available online 8 October 2012

Abstract. Gases in microfluidic structures or devices are often in a non-equilibrium state. The conventional thermodynamic models for fluids and heat transfer break down and the Navier-Stokes-Fourier equations are no longer accurate or valid. In this paper, the extended thermodynamic approach is employed to study the rarefied gas flow in microstructures, including the heat transfer between a parallel channel and pressure-driven Poiseuille flows through a parallel microchannel and circular microtube. The gas flow characteristics are studied and it is shown that the heat transfer in the non-equilibrium state no longer obeys the Fourier gradient transport law. In addition, the bimodal distribution of streamwise and spanwise velocity and temperature through a long circular microtube is captured for the first time.

AMS subject classifications: 76P05, 82B40

Key words: Non-equilibrium, moment method, microchannel, friction coefficient.

1 Introduction

Due to the rapid development in fabrication technology for constructing micro-electro-mechanical systems (MEMS), fluid flow at the micro- and nano-scale has received considerable attention. A basic understanding of the nature of flow and heat transfer in these devices or structures is considered essential for efficient design and control of MEMS. Gas flows in micro-scale devices suffer from non-equilibrium effects when the gas molecular mean free path is the same order as the characteristic length of the device. The degree of

*Corresponding author. *Email address:* ghtang@mail.xjtu.edu.cn (G. H. Tang)

non-equilibrium of a gas is generally expressed through the Knudsen number ($Kn = \lambda/L$) which is the ratio of the molecular mean free path, λ , to a typical dimension of the flow field, L . The different rarefaction regimes can be summarised according to the value of the Knudsen number [1]: (i) no slip ($Kn \leq 10^{-3}$); (ii) slip ($10^{-3} < Kn \leq 10^{-1}$); (iii) transition ($10^{-1} < Kn \leq 10$); and (iv) free molecular flow $Kn > 10$, respectively. Most MEMS operate at the slip and early transition regime ($Kn < 1$) [2]. Different approaches have been employed by various researchers to capture and describe the non-equilibrium phenomena that arise due to an insufficient number of molecular collisions occurring under rarefied conditions. Microscopically, the Boltzmann equation [3] provides an accurate description of a dilute gas at all degrees of rarefaction and describes its state through a molecular distribution function that treats the gas as a large number of interacting molecules, colliding and rebounding according to prescribed laws. However, solutions of the Boltzmann equation, either directly or through the direct simulation Monte Carlo (DSMC) method [4], entail significant mathematical complexity and are computationally expensive, particularly for low-speed, low Knudsen number flows in the slip and transition regime in microchannels.

Due to the difficulties associated with solving the Boltzmann equation, there is significant effort being made to construct alternative solution strategies that can provide an accurate description of a gas with Knudsen numbers that extend into the early transition regime, such as the lattice Boltzmann method (LBM) [5, 6], the discrete-velocity method (DVM) [7–9], the Boltzmann kinetic equation, and the unified gas-kinetic scheme (UGKS) [10]. Among these methods, the extended thermodynamic equations developed with the method of moments, which have been used to predict the hydrodynamic quantities successfully [11–15], is being paid more and more attention.

Grad [16] introduced the moment method for an approximate solution procedure for the Boltzmann equation. He expanded the phase-density distribution function in Hermite polynomials, the coefficients of which are linear combinations of the moments of the molecular distribution function. The 13 moment equations (G13) was first proposed by Grad via truncated distribution function at the third order in Hermite polynomials, which include the five lowest moments of the collision invariants, and stress and heat fluxes proposed by Stokes and Fourier. Struchtrup [17, 18] regularized the G13 equations by using a Chapman-Enskog-like expansion for the closure conditions. The R13 method, which can capture Knudsen layers close to the solid surfaces, is an improvement over the G13 method for some problems [19, 20]. However, the R13 equations cannot capture the Knudsen-layer velocity profile accurately, and overpredict the mass flow rate sometimes [21]. In the present study, a set of 26 moment equations, which are based on the regularizing procedure of Struchtrup for R13 method, are employed by truncating the Hermite polynomials at the fourth order. It is proved to overcome many of the limitations in the R13 method [11]. The R26 method also has limitations. One of the problems by using the regularized moment method is that the equation set, which is a mixed system of the first- and second-order partial differential equations (PDEs), is more complicated. Another problem is that moments higher than second-order have no clear intuitive phys-

ical meaning. That is why moment methods are not well known in the field of continuum fluid dynamics. However, it is able to predict the fluid flow in the early transition regime, and still well known in kinetic theory and provides an alternative solution procedure to the Boltzmann equation with low computational expense.

Analysis of the R26 method for planar Couette flow and force-driven Poiseuille flows has been conducted at previous work. And the set of 26 moment equations is proved effective in the early transition regime. However the existing studies of the moment method are not for non-gradient transport phenomena of heat transfer between parallel channel and pressure-driven flow through a long microchannel, especially for a circular microtube. In this paper, first, the regularised 26 moment equations are briefly introduced. Then, they are employed to study three cases of rarefied gas flow. The temperature profiles and heat transfer are firstly studied for the rarefied gas between two stationary parallel plates at different temperatures. The other two are pressure-driven Poiseuille flows through a long parallel microchannel and a long circular microtube with different outlet Knudsen numbers, respectively.

2 Governing equations

The Boltzmann equation is the central equation in kinetic theory, the properties of which can be used to guide the development of kinetic and macroscopic models for rarefied gas flow. Once the distribution function, f , is known, its moments with respect to the velocity vector, ξ , can be determined. It is convenient to introduce the intrinsic or peculiar velocity as $c_i = \xi_i - u_i$, where ξ_i and u_i represent the particle speed and the local velocity, respectively, so that the moments with respect to u_i can be calculated conveniently. A set of N moments are then used to describe the state of the gas through

$$\rho_{i_1 i_2 \dots i_N} = \int c_{i_1} c_{i_2} \dots c_{i_N} f d\xi. \quad (2.1)$$

The molecular distribution function, f , can be reconstructed from the values of its moments. Grad [16] expressed f in Hermite polynomials as:

$$f = f_M \lim_{N \rightarrow \infty} \sum_{n=0}^N \frac{1}{n!} a_A^{(n)} H_A^{(n)}, \quad (2.2)$$

where $H_A^{(n)}$ are the Hermite polynomials and $a_A^{(n)}$ are the coefficients, which are linear combinations of the moments. f_M is the Maxwellian distribution function. To describe the state of a gas accurately, an infinite number of moments ($N \rightarrow \infty$) is required to reconstruct the distribution function. However, for gases not too far from equilibrium, a finite number of moments should provide an adequate approximation. All the moments included in the truncated distribution function construct the 'Grad moment manifold' (GMM). These moments relax to the equilibrium state at a rate governed by their corresponding governing equations. The remaining higher moments outside the GMM, as

calculated from the truncated distribution function, approach the GMM at a fast finite rate and then relax to the equilibrium state along with the GMM.

2.1 Navier-Stokes-Fourier equations

The traditional hydrodynamic quantities of density ρ , velocity u_i and temperature T correspond to the first five lowest order moments of the molecular distribution function. The governing equations of these hydrodynamic quantities for a dilute gas can be obtained from the Boltzmann equation and represent mass, momentum and energy conservation laws, respectively:

$$\frac{\partial \rho}{\partial t} + \frac{\partial \rho u_i}{\partial x_i} = 0, \quad (2.3)$$

$$\frac{\partial \rho u_i}{\partial t} + \frac{\partial \rho u_i u_j}{\partial x_j} + \frac{\partial \sigma_{ij}}{\partial x_j} = -\frac{\partial p}{\partial x_i} + \rho a_i, \quad (2.4)$$

$$\frac{3}{2}R \frac{\partial \rho T}{\partial t} + \frac{3}{2}R \frac{\partial \rho T u_i}{\partial x_i} + \frac{\partial q_i}{\partial x_i} = -p \frac{\partial u_i}{\partial x_i} - \sigma_{ij} \frac{\partial u_j}{\partial x_i}, \quad (2.5)$$

in which t and x_i are temporal and spatial coordinates, respectively. The external acceleration is denoted by a_i , and pressure, p , is related to the temperature and the density by the ideal gas law $p = \rho RT$, where R is the specific gas constant. To close the set of equations, the stress term σ_{ij} and heat flux q_i are given by a Chapman-Enskog (CE) expansion of the molecular distribution function in terms of Kn around the Maxwellian for Maxwell molecules:

$$\sigma_{ij}^G = -2\mu \frac{\partial u_{\langle i}}{\partial x_{j \rangle}} \quad \text{and} \quad q_i^G = -\frac{15}{4}R\mu \frac{\partial T}{\partial x_i}, \quad (2.6)$$

where μ is the viscosity, and the angular brackets denote the traceless part of a symmetric tensor. Eq. (2.6) expresses an import transport mechanism for u_i and T , and the gradient transport mechanism (GTM), where the superscript G is used to emphasize the importance of this mechanism. If we let

$$\sigma_{ij} = \sigma_{ij}^G \quad \text{and} \quad q_i = q_i^G, \quad (2.7)$$

and insert Eqs. (2.6) and (2.7) into Eqs. (2.4) and (2.5), the results are the traditional hydrodynamic equations, just as the NSF equations. For the NSF equations, the moments included in the GMM are $\{\rho, u_i, T\}$. The CE expansion allows the higher moments σ_{ij} and q_i outside the manifold to deviate from the GMM. The second-order CE expansion adds the non-gradient transport mechanism (NGTM) components to σ_{ij} and q_i and then results in the Burnett equations.

2.2 R13 moment equations

To describe the non-equilibrium phenomenon as the Kn increases, Grad extended the GMM from $\{\rho, u_i, T\}$ to $\{\rho, u_i, T, \sigma_{ij}, q_i\}$, introduced σ_{ij} and q_i as extended variables,

and derived a set of governing equations for them from the Boltzmann equation. For Maxwell molecules, the stress and heat flux equations are shown as:

$$\frac{\partial \sigma_{ij}}{\partial t} + \frac{\partial \sigma_{ij} u_k}{\partial x_k} + \frac{\partial m_{ijk}}{\partial x_k} = -\frac{p}{\mu} \sigma_{ij} - 2p \frac{\partial u_{\langle i}}{\partial x_{j\rangle}} + \Sigma_{ij}, \quad (2.8)$$

$$\frac{\partial q_i}{\partial t} + \frac{\partial q_i u_j}{\partial x_j} + \frac{1}{2} \frac{\partial R_{ij}}{\partial x_j} = -\frac{2}{3} \frac{p}{\mu} q_i - \frac{5}{2} p R \frac{\partial T}{\partial x_i} + Q_i, \quad (2.9)$$

in which

$$\Sigma_{ij} = -2\sigma_{k\langle i} \frac{\partial u_{j\rangle}}{\partial x_k} - \frac{4}{5} \frac{\partial q_{\langle i}}{\partial x_{j\rangle}}, \quad (2.10)$$

$$Q_i = -\frac{7}{2} \sigma_{ik} R \frac{\partial T}{\partial x_k} - RT \frac{\partial \sigma_{ik}}{\partial x_k} + \frac{\sigma_{ij}}{\rho} \left(\frac{\partial p}{\partial x_j} + \frac{\partial \sigma_{jk}}{\partial x_k} \right) - \frac{2}{5} \left(\frac{7}{2} q_k \frac{\partial u_i}{\partial x_k} + q_k \frac{\partial u_k}{\partial x_i} + q_i \frac{\partial u_k}{\partial x_k} \right) - \frac{1}{6} \frac{\partial \Delta}{\partial x_i} - m_{ijk} \frac{\partial u_j}{\partial x_k}. \quad (2.11)$$

Here, m_{ijk} , R_{ij} and Δ represent the differences between the true values of the higher moments and their approximate values with f_{G13} . They are unknown and correspond to

$$m_{ijk} = \rho \langle ij k \rangle, \quad R_{ij} = \rho \langle ij \rangle_{rr} - 7RT \sigma_{ij} \quad \text{and} \quad \Delta = \rho_{rrss} - 15pRT. \quad (2.12)$$

Eqs. (2.3)-(2.5), (2.8) and (2.9) form the 13 moment equations. In Grad's original method, which is the well known G13 equations, such deviations were omitted, so that m_{ijk} , R_{ij} and Δ are set to zero to close the 13 moment equations. Instead, Struchtrup and Torrilhon [17] regularized the G13 equations by applying a Chapman-Enskog-like expansion to the governing equations of the higher moments with linearized production terms for Maxwell molecules and obtained the following closures:

$$m_{ijk} = -2\mu \frac{\partial (\sigma_{ij} / \rho)}{\partial x_k} - \frac{8\mu}{5p} q_{\langle i} \frac{\partial u_{j\rangle}}{\partial x_k}, \quad (2.13)$$

$$R_{ij} = -\frac{24}{5} \mu \frac{\partial (q_{\langle i} / \rho)}{\partial x_{j\rangle}} - \frac{24}{5} \frac{\mu}{p} q_{\langle i} \frac{\partial RT}{\partial x_{j\rangle}} - \frac{24}{7} \frac{\mu}{\rho} \left(\sigma_{k\langle i} \frac{\partial u_{j\rangle}}{\partial x_k} + \sigma_{k\langle i} \frac{\partial u_k}{\partial x_{j\rangle}} - \frac{2}{3} \sigma_{ij} \frac{\partial u_k}{\partial x_k} \right) - \frac{4}{7} \frac{\sigma_{k\langle i} \sigma_{j\rangle k}}{\rho}, \quad (2.14)$$

$$\Delta = -12\mu \frac{\partial (q_k / \rho)}{\partial x_k} - 20 \frac{\mu}{p} q_k \frac{\partial RT}{\partial x_k} - 12 \frac{\mu}{\rho} \sigma_{ij} \frac{\partial u_i}{\partial x_j} - \frac{\sigma_{ij} \sigma_{ij}}{\rho}. \quad (2.15)$$

This set of 13 moment equations with the above closure is the R13 equations. The first terms on the right-hand sides of Eqs. (2.13)-(2.15) provide the GTM for σ_{ij} and q_i and help to stabilize the R13 equations. The gradient transport mechanism of m_{ijk} , R_{ij} and Δ , are

given by

$$m_{ijk}^G = -2\mu \frac{\partial(\sigma_{ij}/\rho)}{\partial x_k}, \quad R_{ij}^G = -\frac{24}{5}\mu \frac{\partial(q_{\langle i}/\rho)}{\partial x_j}, \quad \Delta^G = -12\mu \frac{\partial(q_k/\rho)}{\partial x_k}. \quad (2.16)$$

The rest terms in Eqs. (2.13)-(2.15) represent the NGTM components of the corresponding moments. It is clear that the GTM not only exists for lower-rank moments, but also for higher-rank moments.

2.3 R26 moment equations

Eqs. (2.13) and (2.14) show the relationships for m_{ijk} and R_{ij} . They can only provide a mechanism to produce a boundary layer for the lower-order moments σ_{ij} and q_i but have no mechanism to produce their own boundary layer near the wall [22]. In the present approach, the GTMs for m_{ijk} and R_{ij} near the wall are provided by extending GMM from 13 to 26 moments, which includes the moments m_{ijk} , R_{ij} and Δ as extended hydrodynamic variables. The distribution function is truncated to the incomplete fourth order in Hermite polynomials, and the GMM is extended from $\{\rho, u_i, T, \sigma_{ij}, q_i\}$ to $\{\rho, u_i, T, \sigma_{ij}, q_i, m_{ijk}, R_{ij}, \Delta\}$. From the Boltzmann equation, it is possible to obtain governing equations for m_{ijk} , R_{ij} and Δ for Maxwell molecules as follows:

$$\frac{\partial m_{ijk}}{\partial t} + \frac{\partial u_l m_{ijk}}{\partial x_l} + \frac{\partial \phi_{ijkl}}{\partial x_l} = -\frac{3p}{2\mu} m_{ijk} - 3p \frac{\partial(\sigma_{ij}/\rho)}{\partial x_k} + \mathfrak{M}_{ijk}, \quad (2.17)$$

$$\frac{\partial R_{ij}}{\partial t} + \frac{\partial u_k R_{ij}}{\partial x_k} + \frac{\partial \psi_{ijk}}{\partial x_k} = -\frac{7p}{6\mu} R_{ij} - \frac{28}{5}p \frac{\partial(q_{\langle i}/\rho)}{\partial x_j} + \mathfrak{R}_{ij}, \quad (2.18)$$

$$\frac{\partial \Delta}{\partial t} + \frac{\partial \Delta u_i}{\partial x_i} + \frac{\partial \Omega_i}{\partial x_i} = -\frac{2p}{3\mu} \Delta - 8p \frac{\partial(q_i/\rho)}{\partial x_i} + \mathfrak{X}, \quad (2.19)$$

in which

$$\mathfrak{M}_{ijk} = 3 \frac{\partial \sigma_{\langle ij} \partial \sigma_{k \rangle l}}{\rho \partial x_l} - \frac{12}{5} q_{\langle i} \frac{\partial u_j}{\partial x_k} - 3 m_{l \langle ij} \frac{\partial u_k \rangle}{\partial x_l} - \frac{3}{7} \frac{\partial R_{\langle ij}}{\partial x_k}, \quad (2.20)$$

$$\begin{aligned} \mathfrak{R}_{ij} = & -\frac{2p}{3\mu} \frac{\sigma_{k \langle i} \sigma_{j \rangle k}}{\rho} - \frac{28}{5} q_{\langle i} \frac{\partial RT}{\partial x_j} + \frac{28}{5} \frac{q_{\langle i} \partial \sigma_{j \rangle k}}{\rho \partial x_k} + \frac{14}{3} \frac{\sigma_{ij}}{\rho} \left(\frac{\partial q_k}{\partial x_k} + \sigma_{kl} \frac{\partial u_k}{\partial x_l} \right) - 2RT \frac{\partial m_{ijk}}{\partial x_k} \\ & - 4RT \left(\sigma_{k \langle i} \frac{\partial u_k}{\partial x_j} + \sigma_{k \langle i} \frac{\partial u_j}{\partial x_k} - \frac{2}{3} \sigma_{ij} \frac{\partial u_k}{\partial x_k} \right) - \left(\frac{6}{7} R_{\langle ij} \frac{\partial u_k \rangle}{\partial x_k} + \frac{4}{5} R_{k \langle i} \frac{\partial u_k}{\partial x_j} + 2R_{k \langle i} \frac{\partial u_j \rangle}{\partial x_k} \right) \\ & - 9m_{ijk} \frac{\partial RT}{\partial x_k} - 2\phi_{ijkl} \frac{\partial u_k}{\partial x_l} + 2 \frac{m_{ijk}}{\rho} \left(\frac{\partial p}{\partial x_k} + \frac{\partial \sigma_{kl}}{\partial x_l} \right) - \frac{14}{15} \Delta \frac{\partial u_{\langle i}}{\partial x_j} - \frac{2}{5} \frac{\partial \Omega_{\langle i}}{\partial x_j}, \end{aligned} \quad (2.21)$$

$$\mathfrak{X} = -\frac{2p}{3\mu} \frac{\sigma_{ij} \sigma_{ij}}{\rho} - 4(2RT \sigma_{ij} + R_{ij}) \frac{\partial u_i}{\partial x_j} + 8 \frac{q_i}{\rho} \frac{\partial \sigma_{ij}}{\partial x_j} - 20 q_i \frac{\partial RT}{\partial x_i} - \frac{4}{3} \Delta \frac{\partial u_i}{\partial x_i}. \quad (2.22)$$

Here, ϕ_{ijkl} , ψ_{ijk} and Ω_i are the differences between the true value of the higher moments and their approximated value calculated with f_{G26} . They correspond to

$$\phi_{ijkl} = \rho_{\langle ijkl \rangle}, \quad \psi_{ijk} = \rho_{rr\langle ijk \rangle} - 9RTm_{ijk} \quad \text{and} \quad \Omega_i = \rho_{rrssi} - 28RTq_i. \quad (2.23)$$

If deviations are not allowed for the higher moments away from the GMM, the above equations become a Grad-type 26 moment set of equations. These equations are regularized following the procedure used by Struchtrup. The governing equations for ϕ_{ijkl} , ψ_{ijk} and Ω_i are derived from the Boltzmann equation, and a Chapman-Enskog-like expansion is applied to them. When the nonlinear collision terms are included in these equations, we must take care to ensure that the CE expansion only allow ϕ_{ijkl} , ψ_{ijk} and Ω_i to approach the GMM at a fast rate and then follow the GMM towards the equilibrium state. The 26 moment field equations are closed by

$$\begin{aligned} \phi_{ijkl} = & -\frac{4\mu}{C_1} \frac{\partial(m_{\langle ijk}/\rho)}{\partial x_l} - \frac{12}{C_1} \frac{\mu}{\rho} \sigma_{\langle ij} \frac{\partial u_k}{\partial x_l} + \frac{4\mu}{C_1 p \rho} m_{\langle ijk} \frac{\partial \sigma_{l)m}}{\partial x_m} - \frac{12}{7} \frac{\mu R_{\langle ij}}{C_1 p} \frac{\partial u_k}{\partial x_l} \\ & - \frac{C_2}{C_1} \frac{\sigma_{\langle ij} \sigma_{kl}}{\rho}, \end{aligned} \quad (2.24)$$

$$\begin{aligned} \psi_{ijk} = & -\frac{27\mu}{7Y_1} \frac{\partial(R_{\langle ij}/\rho)}{\partial x_k} - \frac{27}{7} \frac{\mu}{Y_1 p} \left(R_{\langle ij} + 7RT\sigma_{\langle ij} \right) \frac{\partial RT}{\partial x_k} - \frac{108}{5Y_1} \frac{\mu}{\rho} q_{\langle i} \frac{\partial u_j}{\partial x_k} + \frac{27\mu}{7Y_1} \frac{R_{\langle ij}}{p\rho} \frac{\partial \sigma_{k)m}}{\partial x_m} \\ & + \frac{6\mu}{Y_1 p} \frac{m_{ijk}}{\rho} \left(\frac{\partial q_m}{\partial x_m} + \sigma_{ml} \frac{\partial u_m}{\partial x_l} \right) - \frac{\mu}{Y_1 p} \left(\frac{54}{7} m_{m\langle ij} \frac{\partial u_m}{\partial x_k} + 8m_{\langle ijk} \frac{\partial u_m}{\partial x_m} - 6m_{ijk} \frac{\partial u_m}{\partial x_m} \right) \\ & - \left(\frac{Y_2}{Y_1} \frac{\sigma_{\langle li} m_{jkl}}{\rho} + \frac{Y_3}{Y_1} \frac{q_{\langle i} \sigma_{jk}}{\rho} \right), \end{aligned} \quad (2.25)$$

$$\begin{aligned} \Omega_i = & -\frac{7\mu}{3} \frac{\partial(\Delta/\rho)}{\partial x_i} - 4\mu \frac{\partial(R_{ij}/\rho)}{\partial x_j} - \frac{56}{5} \frac{\mu}{\rho} \left(q_j \frac{\partial u_i}{\partial x_j} + q_j \frac{\partial u_j}{\partial x_i} \right) - 8 \frac{\mu}{\rho} m_{ijk} \frac{\partial u_j}{\partial x_k} - 14 \frac{\mu}{p} \\ & \times (2RT\sigma_{ij} + R_{ij}) \frac{\partial RT}{\partial x_j} + \frac{56}{3} \frac{\mu}{p} \frac{q_i}{\rho} \left(\frac{\partial q_j}{\partial x_j} + \sigma_{jk} \frac{\partial u_j}{\partial x_k} \right) + 4 \frac{\mu}{p} \frac{R_{ij}}{\rho} \frac{\partial \sigma_{jk}}{\partial x_k} + \frac{7}{3} \frac{\mu}{p} \Delta \left(\frac{\partial \sigma_{ij}}{\rho \partial x_j} - 2 \frac{\partial RT}{\partial x_i} \right) \\ & - \frac{2}{15} \left(\frac{5m_{ijk} \sigma_{jk} + 14q_j \sigma_{ij}}{\rho} \right), \end{aligned} \quad (2.26)$$

in which, C_1 , C_2 , Y_1 , Y_2 and Y_3 are collision term constants, which have been given in [11]. The first terms on the right-hand side of Eqs. (2.24)-(2.26) provide the GTM for m_{ijk} , R_{ij} and Δ , and play an important role in the region close to the wall. The GTM can be explicitly expressed by

$$\phi_{ijkl}^G = -\frac{4\mu}{C_1} \frac{\partial(m_{\langle ijk}/\rho)}{\partial x_l}, \quad \psi_{ijk}^G = -\frac{27\mu}{7Y_1} \frac{\partial(R_{\langle ij}/\rho)}{\partial x_k} \quad \text{and} \quad \Omega_i^G = -\frac{7\mu}{3} \frac{\partial(\Delta/\rho)}{\partial x_i}. \quad (2.27)$$

The closed set of 26 moment equations is denoted as the R26 moment equations, which is a mixed system of first- and second-order partial differential equations.

2.4 Wall boundary conditions

To construct wall boundary conditions for the R26 equations, a fifth-order approximation of the molecular distribution function, $f^{(5)}$, is required, which is expressed by

$$f^{(5)} = f_M(1 + \varphi), \quad (2.28)$$

in which

$$\begin{aligned} \varphi = & \frac{\sigma_{ij}c_i c_j}{2pRT} + \frac{c_i q_i}{pRT} \left(\frac{c^2}{5RT} - 1 \right) + \frac{m_{ijk}c_i c_j c_k}{6p(RT)^2} + \frac{R_{ij}c_i c_j}{4p(RT)^2} \left(\frac{c^2}{7RT} - 1 \right) + \frac{\psi_{ijk}c_i c_j c_k}{12p(RT)^3} \left(\frac{c^2}{9RT} - 1 \right) \\ & + \frac{\Delta}{8pRT} \left(\frac{c^4}{15(RT)^2} - \frac{2c^2}{3RT} + 1 \right) + \frac{\phi_{ijkl}c_i c_j c_k c_l}{24p(RT)^3} + \frac{c_i \Omega_i}{40p(RT)^2} \left(\frac{c^4}{7(RT)^2} - \frac{2c^2}{RT} + 5 \right), \end{aligned} \quad (2.29)$$

where $c^2 = c_k c_k$. The higher moments involved in Eq. (2.29) are not part of the GMM so that $f^{(5)}$ is not a Grad-type distribution function but a regularized f_{G26} , and is used to construct the WBCs to increase the accuracy near the wall.

Maxwell's kinetic boundary condition [23] is one of the simplest models and it states that a fraction, $(1-\alpha)$, undergoes specular reflection while the remaining fraction, α , is diffusely reflected with a Maxwellian distribution, f_M^w , at the temperature of the wall, T_w . In a frame in which the coordinates are attached to the wall, with n_i the normal vector of the wall pointing towards the gas and τ_i the tangential vector of the wall, such that all molecules with $\xi_i n_i < 0$ are incident upon the wall and molecules with $\xi_i n_i \geq 0$ are emitted by the wall, Maxwell's boundary condition can be expressed by [24]

$$f^w = \begin{cases} \alpha f_M^w + (1-\alpha) f(-\xi_i n_i), & \xi_i n_i \geq 0, \\ f(\xi_i n_i), & \xi_i n_i < 0, \end{cases} \quad (2.30)$$

and

$$f_M = \frac{\rho}{\sqrt{(2\pi RT)^3}} \exp\left(-\frac{c^2}{2RT}\right). \quad (2.31)$$

By definition, the value of any moment at the wall can be obtained from

$$\int_{\xi_i n_i \geq 0} c_{i_1} c_{i_2} \cdots c_{i_n} f(\xi_i n_i) d\xi = \int_{\xi_i n_i \geq 0} c_{i_1} c_{i_2} \cdots c_{i_n} [\alpha f_M^w + (1-\alpha) f(-\xi_i n_i)] d\xi. \quad (2.32)$$

Grad considered the special case of $\alpha = 0$ and concluded that only moments that are odd functions of $c_i n_i$ can be used to construct the wall boundary conditions. This limits the choice of moments to $\psi = (c_n, c_\tau c_n, c^2 c_n, c_\tau^2 c_n, c_n^3, c^2 c_\tau c_n, c_\tau^3 c_n, c_\tau c_n^3, c_\tau^3 c_n^3, c_\tau^4 c_n, c_n^5, c^4 c_n)$, in which $c_n = c_i n_i$ and $c_\tau = c_i \tau_i$. Replace f in Eq. (2.32) with its fifth-order approximation, $f^{(5)}$, and gives the slip velocity, u_τ , parallel to the wall and temperature jump conditions:

$$u_\tau = -\frac{2-\alpha}{\alpha} \sqrt{\frac{\pi RT}{2}} \frac{\sigma_{n\tau}}{p_\alpha} - \frac{5m_{nn\tau} + 2q_\tau}{10p_\alpha} + \frac{9\Omega_\tau + 70\psi_{nn\tau}}{2520p_\alpha RT}, \quad (2.33)$$

$$RT - RT_w = -\frac{2-\alpha}{\alpha} \sqrt{\frac{\pi RT}{2}} \frac{q_n}{2p_\alpha} - \frac{RT\sigma_{nn}}{4p_\alpha} + \frac{u_\tau^2}{4} - \frac{75R_{nn} + 28\Delta}{840p_\alpha} + \frac{\phi_{nnnn}}{24p_\alpha}, \quad (2.34)$$

where

$$p_\alpha = p + \frac{\sigma_{nn}}{2} - \frac{30R_{nn} + 7\Delta}{840RT} - \frac{\phi_{nnnn}}{24RT}. \quad (2.35)$$

Here $\sigma_{nn} = \sigma_{ij}n_i n_j$, $\sigma_{n\tau} = \sigma_{ij}n_i \tau_j$, $q_\tau = q_i \tau_i$, $m_{nn\tau} = m_{ijk}n_i n_j \tau_k$, $m_{nnn} = m_{ijk}n_i n_j n_k$, $R_{nn} = R_{ij}n_i n_j$, $\psi_{nn\tau} = \psi_{ijk}n_i n_j \tau_k$, $\Omega_\tau = \Omega_i \tau_i$ and $\phi_{nnnn} = \phi_{ijkl}n_i n_j n_k n_l$ are tangential and normal components of σ_{ij} , q_i , m_{ijk} , R_{ij} , ψ_{ijk} , Ω_i and ϕ_{ijkl} relative to the wall. Since there is no gas flow through the wall, the normal velocity at the wall keeps at $u_n = 0$. Eqs. (2.33) and (2.34) are similar to the slip velocity and temperature jump conditions for the NSF equations with the underlined terms on the right-hand side providing higher-order moment corrections. The underlined terms can be related to second- or higher-order velocity slip and temperature jump boundary conditions. The second-order velocity-slip boundary condition from Hadjiconstantinou [25] is used in the present work for comparison. The rest of the wall boundary conditions are not listed here. The details can be found in [11].

The variable hard sphere model for argon has been employed with the gas constant $R = 208 \text{ J/kg}\cdot\text{K}$. The molecular mean free path is given by

$$\lambda = \frac{\mu}{p} \sqrt{\frac{\pi RT}{2}}. \quad (2.36)$$

The wall temperature, T_w , and the initial pressure are used as reference values to estimate λ . The viscosity was obtained from Sutherland' law:

$$\mu = \mu_0 \left(\frac{T}{T_0} \right)^{1.5} \frac{T_0 + S}{T + S}, \quad (2.37)$$

where the reference viscosity and temperature are, $\mu_0 = 21.25 \times 10^{-6} \text{ Pa}\cdot\text{s}$ and $T_0 = 273 \text{ K}$, respectively, and the Sutherland's constant, $S = 144 \text{ K}$, for argon.

3 The numerical method

In the moment system, the higher moments provide the transport mechanism for the moments one order lower. The moment method results in a set of equations in a conventional convection-diffusion format, with appropriate source terms, which can be used to capture nonequilibrium phenomena. In most situations, there are no analytical solutions for this complex set of PDEs, and a numerical procedure is therefore required.

3.1 Primitive variable transformation

In the theory of differential equations, variable substitutions or transformations are often used to show that certain classes of equations are equivalent to a standard form. Primitive variables of the governing equations for moments have been transformed during the development of the moment method. The full tensorial moments have been decomposed into their trace and traceless parts and further decomposed into their values on

the GMM and their corresponding deviations. These decompositions are local, and the resultant governing equations are always of a hyperbolic nature regardless of the flow conditions. This is inherited from the streaming part of the Boltzmann equation. However, the collisions at the microscopic level cause the macroscopic quantities of the flow to diffuse. The GTM exists for all the moments considered in the GMM up to 26 moments. The GTM of the low moments are embedded in the moments one order higher. With Eqs. (2.6), (2.16) and (2.27), Eqs. (2.8), (2.9) and (2.17)-(2.19) can be recast in terms of the GTM as

$$\frac{\partial \sigma_{ij}}{\partial t} + \frac{\partial \sigma_{ij} u_k}{\partial x_k} + \frac{\partial m_{ijk}}{\partial x_k} = -\frac{p}{\mu} (\sigma_{ij} - \sigma_{ij}^G) + \Sigma_{ij}, \tag{3.1}$$

$$\frac{\partial q_i}{\partial t} + \frac{\partial q_i u_j}{\partial x_j} + \frac{1}{2} \frac{\partial R_{ij}}{\partial x_j} = -\frac{2}{3} \frac{p}{\mu} (q_i - q_i^G) + Q_i, \tag{3.2}$$

$$\frac{\partial m_{ijk}}{\partial t} + \frac{\partial u_l m_{ijk}}{\partial x_l} + \frac{\partial \phi_{ijkl}}{\partial x_l} = -\frac{3}{2} \frac{p}{\mu} (m_{ijk} - m_{ijk}^G) + \mathfrak{M}_{ijk}, \tag{3.3}$$

$$\frac{\partial R_{ij}}{\partial t} + \frac{\partial u_k R_{ij}}{\partial x_k} + \frac{\partial \psi_{ijk}}{\partial x_k} = -\frac{7}{6} \frac{p}{\mu} (R_{ij} - R_{ij}^G) + \mathfrak{R}_{ij}, \tag{3.4}$$

$$\frac{\partial \Delta}{\partial t} + \frac{\partial \Delta u_i}{\partial x_i} + \frac{\partial \Omega_i}{\partial x_i} = -\frac{2}{3} \frac{p}{\mu} (\Delta - \Delta^G) + \aleph. \tag{3.5}$$

The above set of equations have a common feature in that these moments tend to relax towards the equilibrium state via the values which provide the gradient transport for the moments one order lower, as expressed by the first terms on the right-hand sides of Eqs. (3.2)-(3.5). This phenomenon is clearly caused by the collisions between the molecules. To make full use of the physical aspect of this phenomenon for computation, the moments are decomposed into their GTM and NGTM components defined by

$$\sigma_{ij} = \sigma_{ij}^G + \rho g_{ij}, \quad q_i = q_i^G + \rho h_i, \quad m_{ijk} = m_{ijk}^G + \rho \omega_{ijk}, \tag{3.6a}$$

$$R_{ij} = R_{ij}^G + \rho \gamma_{ij}, \quad \Delta = \Delta^G + \rho \chi, \tag{3.6b}$$

where ρg_{ij} , ρh_i , $\rho \omega_{ijk}$, $\rho \gamma_{ij}$ and $\rho \chi$ are the NGTM components for σ_{ij} , q_i , m_{ijk} , R_{ij} and Δ , respectively. Inserting Eqs. (2.6), (2.16), (2.27), and (3.6) into Eqs. (2.4), (2.5) and (3.1)-(3.5), the governing equations for the new variables are obtained after mathematical manipulation. The primitive variables of the moment equations have been transformed from $\{\rho, u_i, T, \sigma_{ij}, q_i, m_{ijk}, R_{ij}, \Delta\}$ to $\{\rho, u_i, T, g_{ij}, h_i, \omega_{ijk}, \gamma_{ij}, \chi\}$. The resultant equations have the following general convection-diffusion form:

$$\frac{\partial \rho \Phi}{\partial t} + \frac{\partial \rho u_l \Phi}{\partial x_l} - \frac{\partial}{\partial x_l} \left(\frac{\mu}{\Gamma_\Phi} \frac{\partial \Phi}{\partial x_l} \right) = S_\Phi, \tag{3.7}$$

in which $\Phi = \{u_i, T, g_{ij}, h_i, \omega_{ijk}, \gamma_{ij}, \chi\}$; $\Gamma_\Phi = (1, 2/5, 3/2, 5/6, C_1, 7Y_1/9, 3/7)$; and the source terms $S_\Phi = \{S_{u_i}, S_T, S_{g_{ij}}, S_{h_i}, S_{\omega_{ijk}}, S_{\gamma_{ij}}, S_\chi\}$. These equations form a set of second-order PDEs.

3.2 Boundary fitted coordinate systems

For two dimensional flows in Cartesian ($n=0$) or axisymmetric cylindrical ($n=1$) coordinates (x,r) , Eq. (3.7) can be expressed as:

$$\frac{\partial \rho \Phi}{\partial t} + \frac{\partial \rho u \Phi}{\partial x} + \frac{\partial r^n \rho v \Phi}{r^n \partial r} - \frac{\partial}{\partial x} \left(\frac{\mu}{\Gamma_\Phi} \frac{\partial \Phi}{\partial x} \right) - \frac{\partial}{\partial r} \left(\frac{r^n \mu}{\Gamma_\Phi} \frac{\partial \Phi}{\partial r} \right) = S_\Phi. \tag{3.8}$$

Use a curvilinear coordinate transformation to map the complex flow domain in physical space to a simple flow domain in computational space. The Cartesian coordinate system $x_i=(x,r)$ in the physical domain is replaced by a curvilinear coordinate system $\xi_i=(\xi,\eta)$ such that boundaries of the flow domain correspond to surface $\xi_i=\text{constant}$. Eq. (3.8) can be transformed to a general curvilinear system (ξ,η) :

$$\frac{\partial \Phi}{\partial x} = \frac{1}{J} \left(y_\eta \frac{\partial \Phi}{\partial \xi} - y_\xi \frac{\partial \Phi}{\partial \eta} \right) \quad \text{and} \quad \frac{\partial \Phi}{\partial r} = \frac{1}{J} \left(-x_\eta \frac{\partial \Phi}{\partial \xi} + x_\xi \frac{\partial \Phi}{\partial \eta} \right), \tag{3.9}$$

where $J = x_\xi y_\eta - x_\eta y_\xi$ is the Jacobean coefficient and

$$x_\xi = \frac{\partial x}{\partial \xi}, \quad x_\eta = \frac{\partial x}{\partial \eta}, \quad y_\xi = \frac{\partial r}{\partial \xi}, \quad y_\eta = \frac{\partial r}{\partial \eta}. \tag{3.10}$$

The transformed equation has the general form of

$$r^n J \frac{\partial \rho \Phi}{\partial t} + \frac{\partial r^n \rho G_1 \Phi}{\partial \xi} + \frac{\partial r^n \rho G_2 \Phi}{\partial \eta} - \frac{\partial}{\partial \xi} \left(\frac{r^n \omega \mu}{\Gamma_\Phi} \frac{\partial \Phi}{\partial \xi} \right) - \frac{\partial}{\partial \eta} \left(\frac{r^n \gamma \mu}{\Gamma_\Phi} \frac{\partial \Phi}{\partial \eta} \right) = r^n J S_\Phi + D_\Phi^{cr} \tag{3.11}$$

with $G_1 = uy_\eta - vx_\eta$, $G_2 = vx_\xi - uy_\xi$ and

$$D_\Phi^{cr} = -\frac{\mu}{\Gamma_\Phi} \left[(\omega y_\xi + x_\eta) \frac{\partial \Phi}{\partial \xi} + (\gamma y_\eta - x_\xi) \frac{\partial \Phi}{\partial \eta} \right] - r^n \left[\frac{\partial}{\partial \xi} \left(\frac{\mu \beta}{\Gamma_\Phi} \frac{\partial \Phi}{\partial \eta} \right) + \frac{\partial}{\partial \eta} \left(\frac{\mu \beta}{\Gamma_\Phi} \frac{\partial \Phi}{\partial \xi} \right) \right], \tag{3.12}$$

in which

$$\omega = \frac{x_\eta^2 + y_\eta^2}{J}, \quad \beta = \frac{x_\xi x_\eta + y_\xi y_\eta}{J} \quad \text{and} \quad \gamma = \frac{x_\xi^2 + y_\xi^2}{J}. \tag{3.13}$$

3.3 The discretization procedure

A collocate, rather staggered, grid approach is adopted, which stores all variables at the same grid points $WW, W, P, E, EE, SS, S, N$, and NN , as shown in Fig. 1. All the transport equations are formulated and discretized in the curvilinear coordinates with the finite volume method in (ξ,η) domain. A discrete approximation to Eq. (3.11), for

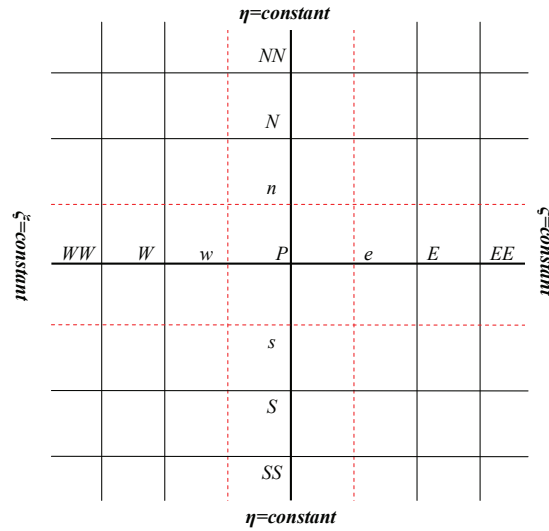


Figure 1: Collocated grid arrangement.

any variable, Φ , is achieved by integrating the equation over a macro-control volume surrounding the nodal point P ,

$$\int_s^n \int_w^e \left[\frac{\partial r^n \rho G_1 \Phi}{\partial \zeta} - \frac{\partial}{\partial \zeta} \left(\frac{r^n \omega \mu}{\Gamma_\Phi} \frac{\partial \Phi}{\partial \zeta} \right) \right] d\zeta d\eta + \int_s^n \int_w^e \left[\frac{\partial r^n \rho G_2 \Phi}{\partial \eta} - \frac{\partial}{\partial \eta} \left(\frac{r^n \gamma \mu}{\Gamma_\Phi} \frac{\partial \Phi}{\partial \eta} \right) \right] d\zeta d\eta = \int_s^n \int_w^e (r^n JS_\Phi + D_\Phi^{cr}) d\zeta d\eta, \tag{3.14}$$

where n, s, e and w refer to the location of the space average of any quantity prevailing over the faces of the control volume. Using the mean-value theorem, Eq. (3.14) can be written as:

$$\left[\left(r^n \rho G_1 \Phi - \frac{r^n \omega \mu}{\Gamma_\Phi} \frac{\partial \Phi}{\partial \zeta} \right)_e - \left(r^n \rho G_1 \Phi - \frac{r^n \omega \mu}{\Gamma_\Phi} \frac{\partial \Phi}{\partial \zeta} \right)_w \right] \delta\eta + \left[\left(r^n \rho G_2 \Phi - \frac{r^n \gamma \mu}{\Gamma_\Phi} \frac{\partial \Phi}{\partial \eta} \right)_n - \left(r^n \rho G_2 \Phi - \frac{r^n \gamma \mu}{\Gamma_\Phi} \frac{\partial \Phi}{\partial \eta} \right)_s \right] \delta\zeta = \int_s^n \int_w^e (r^n JS_\Phi + D_\Phi^{cr}) d\zeta d\eta. \tag{3.15}$$

This equation expresses the balance between the net influx of the flow property under consideration through the volume surface, the property's volumetric rate of accumulation and its volumetric rate of generation. A finite difference equation (FDE), linking the value of Φ at P to its value at neighbouring nodes ($EE, E, WW, W, NN, N, SS, S$) is constructed under the following assumptions:

- (1) $(r^n JS_\Phi + D_\Phi^{cr})$ is taken to be uniform over the cell volume and has the following linearised form $\int_s^n \int_w^e (r^n JS_\Phi + D_\Phi^{cr}) d\zeta d\eta = S_s + S_P \Phi_P$;

- (2) Standard central differencing is used to discretize any term in $(r^n JS_\Phi + D_\Phi^{cr})$, and S_p is chosen to have a negative sink in order to make the resulting matrix more diagonally dominant;
- (3) For the diffusion terms, Φ is taken to vary linearly between nodes;
- (4) For the convection terms, the face values, Φ_s, Φ_n, Φ_w and Φ_e are approximated by

$$\Phi_w = \beta_w^{WW} \Phi_{WW} + \beta_w^W \Phi_W + \beta_w^P \Phi_P + \beta_w^E \Phi_E, \tag{3.16a}$$

$$\Phi_e = \beta_e^W \Phi_W + \beta_e^P \Phi_P + \beta_e^E \Phi_E + \beta_e^{EE} \Phi_{EE}, \tag{3.16b}$$

$$\Phi_s = \beta_s^{SS} \Phi_{SS} + \beta_s^S \Phi_S + \beta_s^P \Phi_P + \beta_s^N \Phi_N, \tag{3.16c}$$

$$\Phi_n = \beta_n^S \Phi_S + \beta_n^P \Phi_P + \beta_n^N \Phi_N + \beta_n^{NN} \Phi_{NN}, \tag{3.16d}$$

where β represents the rating factors depending on the numerical scheme used. Here the CUBISTA scheme was selected for the present work. The resulting general FDE is

$$(A_P - S_P) \Phi_P = \sum_{i=E,W,N,S,EE,WW,NN,SS} A_i \Phi_i + S_s, \tag{3.17}$$

where Φ_i is the value of Φ at point i ($i = E, W, N, S, EE, WW, NN, SS$) and

$$A_w = D_w + C_w \beta_w^W - C_e \beta_e^W, \quad A_E = D_e - C_e \beta_e^E + C_w \beta_w^E, \tag{3.18a}$$

$$A_S = D_s + C_s \beta_s^S - C_n \beta_n^S, \quad A_N = D_n - C_n \beta_n^N - C_s \beta_s^N, \tag{3.18b}$$

$$A_{WW} = C_w \beta_w^{WW}, \quad A_{EE} = -C_e \beta_e^{EE}, \quad A_{SS} = C_s \beta_s^{SS}, \quad A_{NN} = -C_n \beta_n^{NN}. \tag{3.18c}$$

Here D and C are diffusion and convection fluxes across the control volume faces ($\delta\xi=1, \delta\eta=1$):

$$C_e = (r^n \rho)_e G_{1e}, \quad C_w = (r^n \rho)_w G_{1w}, \quad C_n = (r^n \rho)_n G_{2n}, \quad C_s = (r^n \rho)_s G_{2s}, \tag{3.19a}$$

$$D_e = (r^n \varpi \mu)_e, \quad D_w = (r^n \varpi \mu)_w, \quad D_n = (r^n \gamma \mu)_n, \quad D_s = (r^n \gamma \mu)_s. \tag{3.19b}$$

3.4 Solution of the algebraic equations

When equations similar to Eq. (3.17) are constructed at each of the computational grid point covering the solution domain, a coefficient matrix is obtained for the variable Φ . The transport coefficients and source coefficients may themselves depend on the solution for any one or more of the dependent variables. The solution of this set of non-linear algebraic equations can be obtained by an iterative method. Here a line-by-line 'Penta-Diagonal-Matrix-Algorithm' (PDMA) is employed to solve Eq. (3.17) with a double sweep in each coordinate direction. The change of coefficients A and Φ , between iterations, may result in large variations with a consequent slowing of convergence and/or even divergence. The convergence rate can be improved by 'off-line successive relaxation'. If a relaxation factor ϑ is used in order to reduce the variation in Φ , Eq. (3.17) becomes:

$$\frac{A_P}{\vartheta} \Phi_P = \sum A_i \Phi_i + S_s + \frac{1-\vartheta}{\vartheta} A_P \Phi_P^* \tag{3.20}$$

with $A_P = \sum A_i - S_P$. The superscript * denotes the value at the previous iteration. A value of θ between zero and unity or greater than unity is equivalent to under-relaxation or over-relaxation respectively. Under relaxation is a very useful device for avoiding divergence during the iteration of strongly nonlinear equations. When the iterations converge, Φ becomes equal to Φ^* . Eq. (3.20) ensures that the converged values of Φ do satisfy the original Eq. (3.17).

3.5 Pressure-velocity coupling

The coupling of the velocity and pressure fields is through the Semi-Implicit Pressure-Linked Equation (SIMPLE) algorithm [26]. A collocated grid arrangement, which can give rise to spurious pressure oscillations and present an additional challenge for the implementation of second-moment turbulence closures, is used in the present study. The interpolation scheme of Rhie and Chow [27] is employed to eliminate any non-physical pressure oscillations.

Application of Eq. (3.17) to the velocity u for the control volume at P gives

$$A_P^u u_P = \sum A_i u_i + S^u + B_P^u (p_e - p_w) + C_P^u (p_n - p_s), \quad (3.21)$$

where S^u is the source term, except pressure, in the u equation. The face area coefficients are shown as:

$$B_P^u = -(y_\eta r^n)_P \quad \text{and} \quad C_P^u = (y_\xi r^n)_P. \quad (3.22)$$

Since the pressure field is generally unknown, a pressure distribution p^* is assumed, which, when substituted into Eq. (3.21), yields the corresponding approximate velocity field u^* ,

$$A_P^u u_P^* = \sum A_i u_i^* + S^u + B_P^u (p_e^* - p_w^*) + C_P^u (p_n^* - p_s^*). \quad (3.23)$$

If u and p are the correct solutions of velocity and pressure field, then:

$$u = u^* + u' \quad \text{and} \quad p = p^* + p', \quad (3.24)$$

where u' and p' are the corrections to the current velocity and pressure. Subtracting Eq. (3.23) from Eq. (3.21) gives

$$A_P^u u'_P = \sum A_i u'_i + B_P^u (p'_e - p'_w) + C_P^u (p'_n - p'_s). \quad (3.25)$$

The SIMPLE algorithm neglected the first term on the right hand side of Eq. (3.23) to give the following simplified expression:

$$u_P = u_P^* + \frac{B_P^u}{A_P^u} (p'_e - p'_w) + \frac{C_P^u}{A_P^u} (p'_n - p'_s). \quad (3.26)$$

An analogous expression for v is easily obtained,

$$v_P = v_P^* + \frac{B_P^v}{A_P^v} (p'_e - p'_w) + \frac{C_P^v}{A_P^v} (p'_n - p'_s), \quad (3.27)$$

in which

$$B_P^v = (x_\eta r^n)_P \quad \text{and} \quad C_P^v = -(x_\xi r^n)_P. \quad (3.28)$$

Inserting Eqs. (3.26) and (3.27) into $G_1 = uy_\eta - vx_\eta$ and $G_2 = vx_\xi - uy_\xi$ gives

$$G_{1P} = G_{1P}^* + Q_P (p'_e - p'_w) + E_P (p'_n - p'_s), \quad (3.29a)$$

$$G_{2P} = G_{2P}^* + F_P (p'_e - p'_w) + H_P (p'_n - p'_s), \quad (3.29b)$$

in which

$$Q_P = \frac{B_P^u}{A_P^u} y_\eta - \frac{B_P^v}{A_P^v} x_\eta, \quad E_P = \frac{C_P^u}{A_P^u} y_\eta - \frac{C_P^v}{A_P^v} x_\eta, \quad (3.30a)$$

$$F_P = \frac{B_P^v}{A_P^v} x_\xi - \frac{B_P^u}{A_P^u} y_\xi, \quad H_P = \frac{C_P^v}{A_P^v} x_\xi - \frac{C_P^u}{A_P^u} y_\xi. \quad (3.30b)$$

For the control volume centered at P , the discretized continuity equation can be expressed as

$$C_e - C_w + C_n - C_s = 0, \quad (3.31)$$

in which the values of G_{1e} , G_{1w} , G_{2n} and G_{2s} are required. Following the same procedure for G_{1P} and G_{2P} , it is readily to obtain:

$$G_{1w} = G_{1w}^* + Q_w (p'_P - p'_W) + \frac{1}{4} E_P (p'_N - p'_S) + \frac{1}{4} E_W (p'_N - p'_S)_W, \quad (3.32a)$$

$$G_{1e} = G_{1e}^* + Q_e (p'_E - p'_P) + \frac{1}{4} E_E (p'_N - p'_S)_E + \frac{1}{4} E_P (p'_N - p'_S), \quad (3.32b)$$

$$G_{2s} = G_{2s}^* + H_s (p'_P - p'_S) + \frac{1}{4} F_P (p'_E - p'_W) + \frac{1}{4} F_S (p'_E - p'_W)_S, \quad (3.32c)$$

$$G_{2n} = G_{2n}^* + H_n (p'_N - p'_P) + \frac{1}{4} F_N (p'_E - p'_W)_N + \frac{1}{4} F_P (p'_E - p'_W), \quad (3.32d)$$

in which

$$Q_w = \frac{Q_W + Q_P}{2}, \quad Q_e = \frac{Q_E + Q_P}{2}, \quad H_s = \frac{H_S + H_P}{2}, \quad H_n = \frac{H_N + H_P}{2}, \quad (3.33a)$$

$$G_{1w}^* = \frac{G_{1W}^* + G_{1P}^*}{2}, \quad G_{1e}^* = \frac{G_{1E}^* + G_{1P}^*}{2}, \quad G_{2s}^* = \frac{G_{2S}^* + G_{2P}^*}{2}, \quad G_{2n}^* = \frac{G_{2N}^* + G_{2P}^*}{2}. \quad (3.33b)$$

By introducing Eq. (3.32) into Eqs. (3.19) and (3.31), the following pressure correction equation is obtained:

$$A_P p'_P = \sum A_i p'_i + S_1 + S_2, \quad (3.34)$$

in which

$$A_E = (r^n \rho)_e Q_e + R_2, \quad A_W = (r^n \rho)_w Q_w - R_2, \quad (3.35a)$$

$$A_N = (r^n \rho)_n H_n + R_1, \quad A_S = (r^n \rho)_s H_s - R_1, \quad (3.35b)$$

$$R_1 = \frac{1}{4} E_P [(r^n \rho)_e - (r^n \rho)_w], \quad R_2 = \frac{1}{4} F_P [(r^n \rho)_n - (r^n \rho)_s], \quad (3.35c)$$

$$A_P = A_E + A_W + A_N + A_S, \quad (3.35d)$$

$$S_1 = (r^n \rho)_e G_{1e}^* - (r^n \rho)_w G_{1w}^* - \frac{1}{4} [(r^n \rho)_e E_E (p'_N - p'_S)_E - (r^n \rho)_w E_W (p'_N - p'_S)_W], \quad (3.35e)$$

$$S_2 = (r^n \rho)_n G_{2n}^* - (r^n \rho)_s G_{2s}^* - \frac{1}{4} [(r^n \rho)_n F_N (p'_E - p'_W)_N - (r^n \rho)_s F_S (p'_E - p'_W)_S]. \quad (3.35f)$$

The solution of p' from Eq. (3.34) updates the pressure and velocity through Eqs. (3.26), (3.27), (3.29) and (3.32). However, the pressure field obtained from the above approach in the collocated grid has spurious oscillations. This is caused by the interpolation of the values of G_1 and G_2 at the control volume faces. To overcome this, the linear interpolation of the values of G_1 and G_2 at the control volume faces in Eq. (3.33) is replaced by the interpolation scheme of Rhie and Chow:

$$G_{1w}^* = \frac{G_{1P}^* + G_{1W}^*}{2} - \frac{1}{4} [Q_P (p_E - p_W) + Q_W (p_P - p_{WW})] + Q_w (p_P - p_W). \quad (3.36)$$

By doing so, G_{1w}^* is proportional to $Q_W (p_P - p_W)$ rather than to $Q_P (p_E - p_W) + Q_W (p_P - p_{WW})$ which is implicitly included in the first term in the right hand side of Eq. (3.36). The boundary values of both p' and p are obtained by the extrapolation along the curvilinear coordinates with

$$\left(\frac{\partial^2 p'}{\partial s^2} \right)_{\xi=c, \text{or}, \eta=c} = 0 \quad \text{and} \quad \left(\frac{\partial^2 p}{\partial s^2} \right)_{\xi=c, \text{or}, \eta=c} = 0. \quad (3.37)$$

The solution procedure is summarized as follows:

- (1) Solve u_i at iteration $n+1$ using the values of other variables at the previous iteration n .
- (2) Solve the pressure correction equation using the SIMPLE algorithm to update p and u_i at iteration $n+1$.
- (3) Solve T , g_{ij} , h_i , ω_{ijk} , γ_{ij} , χ at iteration $n+1$ using updated pressure and velocity fields.
- (4) Calculate values of the moments σ_{ij} , q_i , m_{ijk} , R_{ij} and Δ .
- (5) Update the boundary conditions.
- (6) Return to step (1) and repeat until residuals of each governing equation reach a specified convergence criterion.

4 Numerical results

4.1 Heat transfer between a parallel channel

In this section, the heat transfer between two parallel plates with different temperatures is studied with the extended thermodynamic model. To be consistent with the DSMC simulation [28], the lower wall with a temperature of 263K sits at $y = 0$ and the upper wall with a temperature of 283K at $y = H$. H is fixed at 1mm. All the derivatives in the x -direction parallel to the walls are zero. Both walls are stationary. The Knudsen number is calculated at a reference temperature of 273K and different reference pressures, as given in [28]. The predicted temperature profiles at different Knudsen numbers are shown in Fig. 2 in comparison with the DSMC data [28]. When $Kn = 0.0475$ in the slip regime, both NSF and extended thermodynamic models can predict the temperature between the plates accurately, except that the NSF equations cannot capture the thermal Knudsen layer close to the walls as shown in Fig. 2(a). As the Knudsen number increases, the NSF equations with the temperature jump condition overpredict the temperature jump significantly while the 26 moment equations are in rough agreement with the DSMC data, as shown in Figs. 2(b) and (c). In addition, predictions for the temperature of the 26 moment equations are a little better than those of the 13 moment equations. When Kn is larger than 1, both macroscopic models fail to predict the temperature profile, and results predicted by the 13 moment equations are unavailable during our numerical computation which are not shown in the figures.

The normal heat flux, q_y , between two plates is a constant as shown in Fig. 3(a). However the NSF equations underpredict the value of heat flux as the Knudsen number increases. Compared to 26 moment equations, the 13 moment equations overpredict the value of heat flux. The NSF equations predict a constant pressure distribution between the two plates. However, the 26 moment equations show that the pressure close to the hot wall is higher than that close to the cold wall, as demonstrated in Fig. 3(b). More interestingly, the normal stresses, σ_{xx} and σ_{yy} are not equal to zero even without any velocity gradient and the NSF equations completely fail to capture this non-equilibrium effect as indicated in Fig. 3(c).

4.2 Pressure driven gas flow in a long parallel microchannel

Pressure-driven gas flow through a long microchannel, which has wide applications in MEMS, is studied with the extended thermodynamic model. The walls with a temperature of $T_0 = 273\text{K}$ sit at $y = 0$ and $y = H$ separately. The height of the channel, H , is $1\mu\text{m}$ and the ratio of the channel length, L , to height keeps at 100. Pressure ratio P_i of the inlet to outlet is 2.0. Knudsen number is calculated based on the temperature of 273K and the outlet pressure p_e . The predicted velocity and pressure profiles at different outlet Knudsen numbers are shown in Fig. 4 in comparison with the R13 data and DSMC data [29, 30]. The streamwise velocity is normalized by the maximum streamwise veloc-

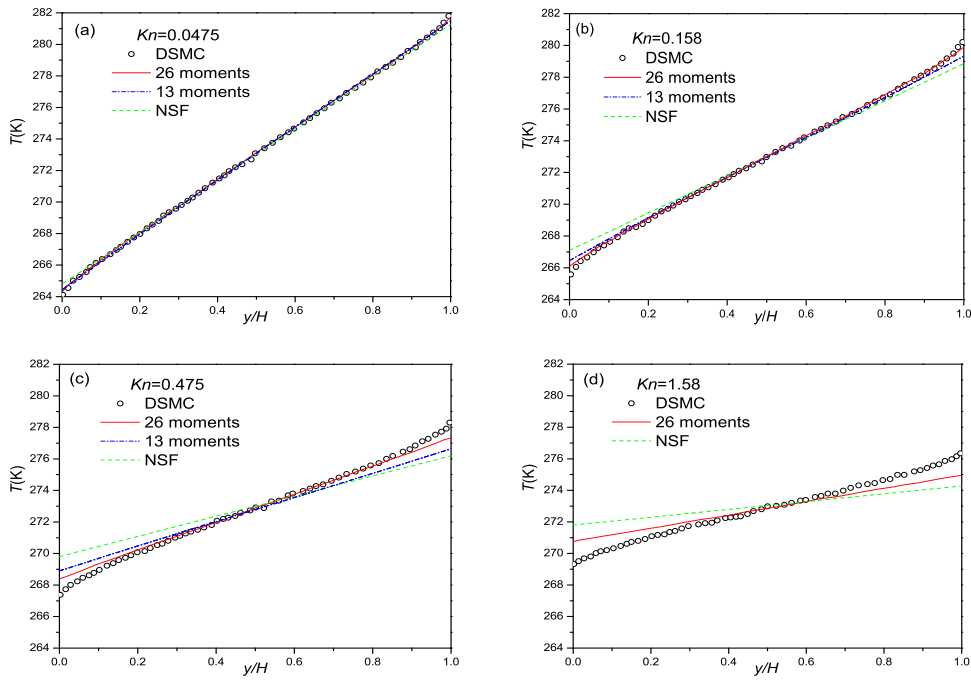


Figure 2: Predicted temperature profile between two parallel plates with different temperatures at different values of Knudsen numbers. DSMC data are digitised from [28].

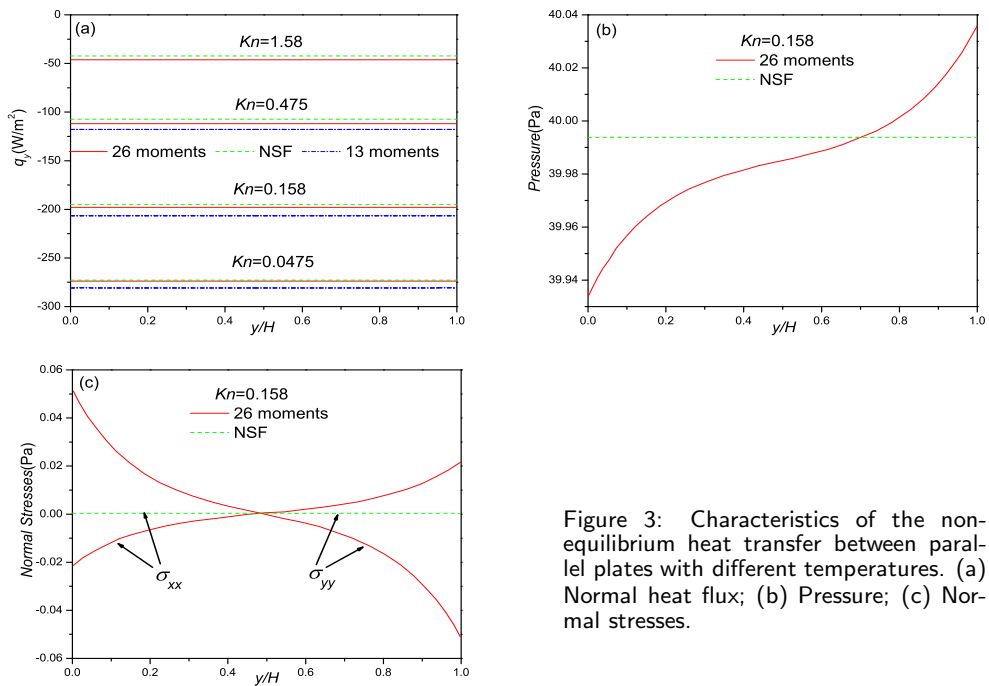


Figure 3: Characteristics of the non-equilibrium heat transfer between parallel plates with different temperatures. (a) Normal heat flux; (b) Pressure; (c) Normal stresses.

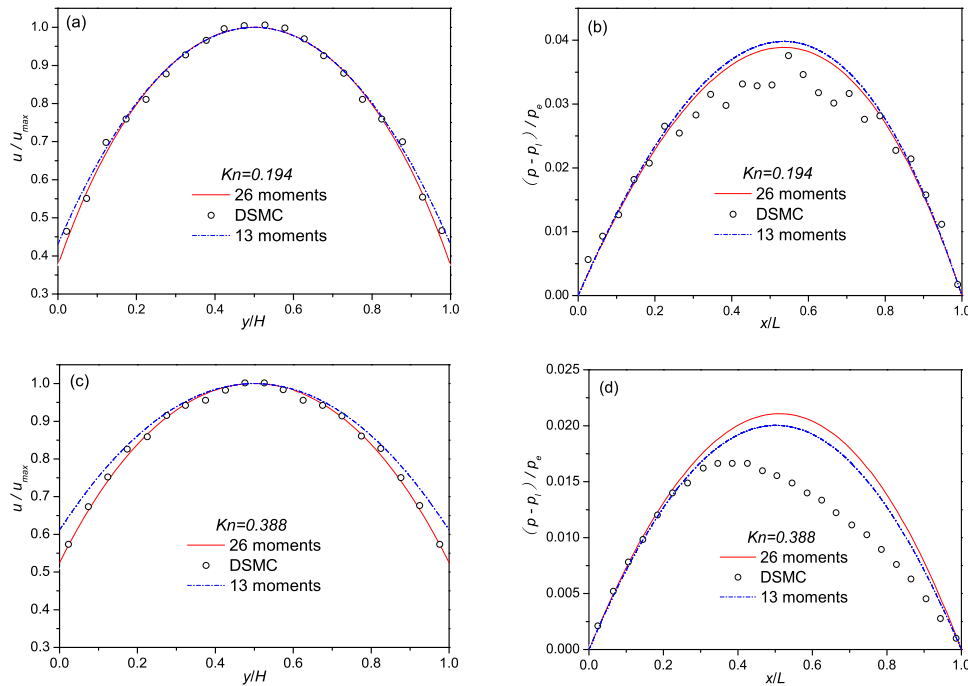


Figure 4: Streamwise velocity at the outlet and streamwise pressure deviation from a linear distribution for pressure-driven flow through a long microchannel. (a, b) $Kn=0.194$; (c, d) $Kn=0.388$.

ity u_{max} at the outlet, and the pressure $p - p_1$, which presents the pressure deviation from linear pressure drop corresponding to incompressible laminar flow, is normalized by the outlet pressure. The velocity profiles from the 26 moment equations are in good agreement with the DSMC data as shown in Figs. 4(a) and (c). There is a little deviation of the velocity profiles from the 13 moment equations compared to those of the 26 moment equations and DSMC data. As shown in Fig. 4(c) at $Kn = 0.388$, the 13 moment equations overpredict the velocity slip at the wall. Deviation of the pressure distribution from a linear pressure can also be captured by the extended thermodynamic model. In Fig. 4(b), when $Kn = 0.194$, the pressure distributions from the 13 moments and 26 moments are in rough agreement with the DSMC data. When the Kn increases, as shown in Fig. 4(d), both moment methods fail to capture the pressure distribution. It is interesting that the pressure distribution by the 13 moment equations even agrees better than that by the 26 moments at $Kn = 0.388$. Considering the velocity distribution by the 13 moments at $Kn = 0.388$, the pressure distribution may not be used solely to evaluate the accuracy of the extended thermodynamic models.

The Knudsen number and pressure ratio of the inlet to outlet have important impact on the profiles of pressure in the microchannel with pressure boundary condition. When Kn is fixed at 0.194, the effect of the pressure ratio is shown in Fig. 5(a). As the pressure ratio increases, deviation of the pressure distribution from a linear pressure decreases.

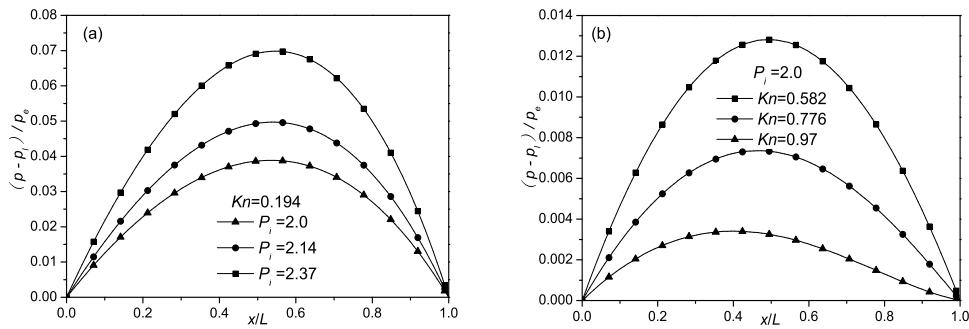


Figure 5: Pressure profiles along the streamwise direction with different pressure ratios and Knudsen numbers. (a) $Kn=0.194$; (b) $P_i=2.0$.

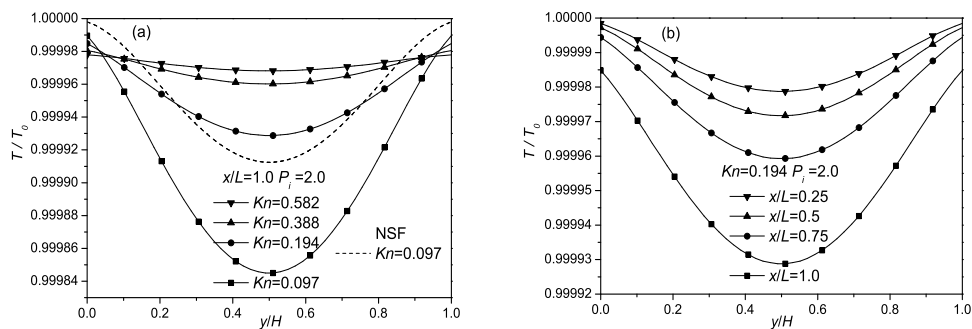


Figure 6: Distribution of the dimensionless temperature along the y -direction. (a) At different Knudsen numbers; (b) At different streamwise locations.

Fig. 5(b) shows the effect of the increasing Kn when pressure ratio is fixed at 2.0. It can be observed that the stronger the rarefaction effect, as indicated by the larger value of Kn , the smaller the deviation from the linear pressure distribution and also the peak of the curve moves toward the inlet of the microchannel slightly. This means that the rarefaction effect serves to decrease the curvature in the pressure distribution caused by the compressibility effect. Thus the effect of the compressibility and the effect of the rarefaction on the pressure distribution are contrary. Generally speaking, the two effects are not equal, resulting in a nonlinear pressure distribution.

The profiles of temperature along the y -direction are also shown in Fig. 6. From Fig. 6 we can see that the gas temperature is less than the reference temperature T_0 . The centre temperature is slightly lower than that near the wall along the y -direction and the temperature gradient increases along the streamwise direction, since the viscous heating is surpassed by the expansion cooling, especially in the outlet region. In addition, the temperature gradient decreases as the Knudsen number increases. As the Knudsen number increases, both the jump temperature and the slip velocity at the wall increase. The increased jump temperature results in a marked decrease in wall temperature gradient while the increase in wall temperature gradient caused by the increased slip velocity

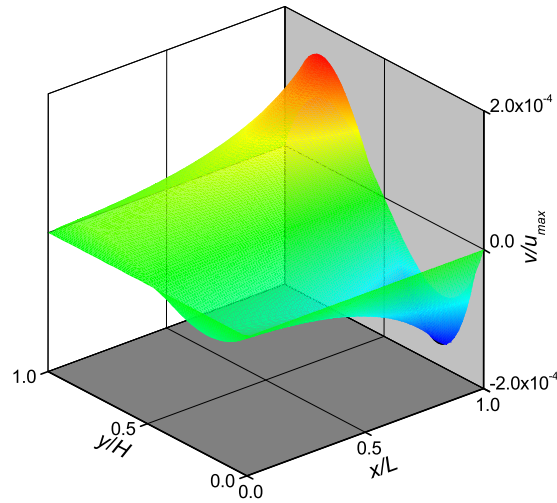


Figure 7: Spanwise velocity for pressure-driven flow through a long microchannel at $Kn=0.194$ and $P_i=2.0$.

is not evident. Thus the expansion cooling heat transfer effect decreases due to the increased thermal resistance. However, the temperature variation in Fig. 6 is quite small on the scale of 10^{-5} , and further studies by using other numerical methods are still needed for verification.

The spanwise velocity of a gas in the microchannel normalized by u_{max} is shown in Fig. 7 when $Kn=0.194$ and $P_i=2.0$. The value of spanwise velocity is smaller substantially than that of the streamwise velocity. However, the trend of the gas flowing from the channel centerline toward the wall is observed. These observations are in consistent with previous analytical solutions for microflows in a long channel qualitatively [31].

The friction coefficient is defined as

$$f = \frac{2\tau_w}{\rho u_{av}^2}. \tag{4.1}$$

Here τ_w is the shear stress at the wall, and u_{av} is the average velocity along the y -direction. Multiplying the friction coefficient by Reynolds number, the Poiseuille number (fRe) can be obtained by computing with the macroscopic expression with different slip velocity models [32],

$$fRe = \frac{24}{1 + 6A_1Kn + 12A_2Kn^2}. \tag{4.2}$$

A_1 and A_2 are the coefficients of various slip velocity models. In addition, we can also derive the following equation [33]

$$fRe = \frac{2\sqrt{\pi}}{KnQ}. \tag{4.3}$$

Here Q is the non-dimensional flow rate decided by the linearized Boltzmann solution for parallel channel [34]. Fig. 8 shows the relation between the fRe and Kn in the streamwise

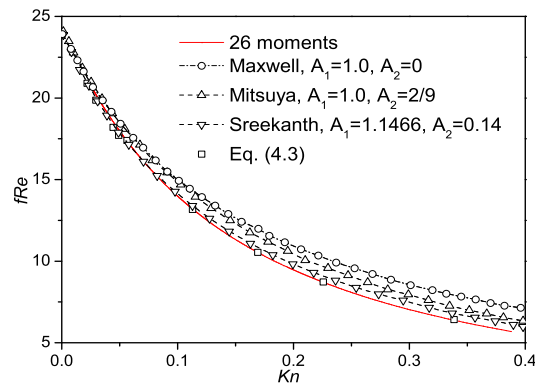


Figure 8: The Poiseuille number against the Knudsen number in a long parallel microchannel, compared with the linearized Boltzmann equation solution [34] and macroscopic equation with different slip velocity models [32].

direction. The present numerical results of 26 moment method agree well with Eq. (4.3) in which the non-dimensional flow rate data from the linearized Boltzmann equation solution are used. The second-order slip model of the Sreekanth's model with $A_1 = 1.1466$ and $A_2 = 0.14$ is also in rough agreement with the present numerical results, followed by the Mitsuya model. The first-order Maxwell slip model deviates the largest.

4.3 Pressure-driven gas flow in a long circular microtube

Pressure-driven gas flow through a long microtube is also studied with the extended thermodynamic model. The wall with a temperature of 273K sits at $y = R$, and the centreline of the tube sits at $y = 0$. The radius of the tube, R , is $1\mu\text{m}$ and the ratio of the channel length, L , to height keeps at 50. The pressure ratio, P_i , of the inlet to outlet is 2.0. The Knudsen number is calculated based on the temperature of 273K, the pressure at the outlet, and the diameter $2R$.

The profiles of predicted velocity at different Knudsen numbers are shown in Fig. 9(a) in comparison with the data calculated by the NSF equations with the second-order boundary conditions. The streamwise velocity is normalized by the average velocity u_{av} of the corresponding cross-section. The numerical results of the 26 moment method show that, as the Knudsen number increases, two peaks appear in the distribution of the streamwise velocity. This bimodal distribution is unlike the velocity distribution in the pressure-driven parallel channel flow. For rarefied gas flow, the velocity is made up of the velocity slip, the Knudsen layer velocity and the bulk velocity. The R26 equations are able to capture the Knudsen layer velocity profile due to the tangential heat flow and the extra boundary layer contribution from m_{ijk} . The Knudsen layer velocity, which behaves similar bimodal distribution, is responsible for this unique phenomenon. As shown in Fig. 9(a), the NSF equations fail to capture the bimodal profiles. Note that the NSF results for $Kn = 0.5$ and 0.7 are not presented here for comparison since they deviate from the results of the 26 moment equations too much. In addition, the profiles of predicted

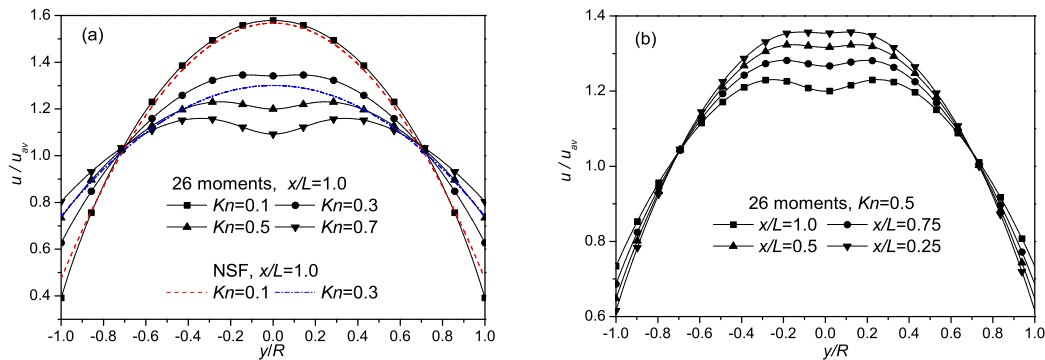


Figure 9: Distribution of the streamwise velocity in the microtube. (a) Compared with the NSF data at various Knudsen numbers. (b) At different streamwise positions when $Kn=0.5$.

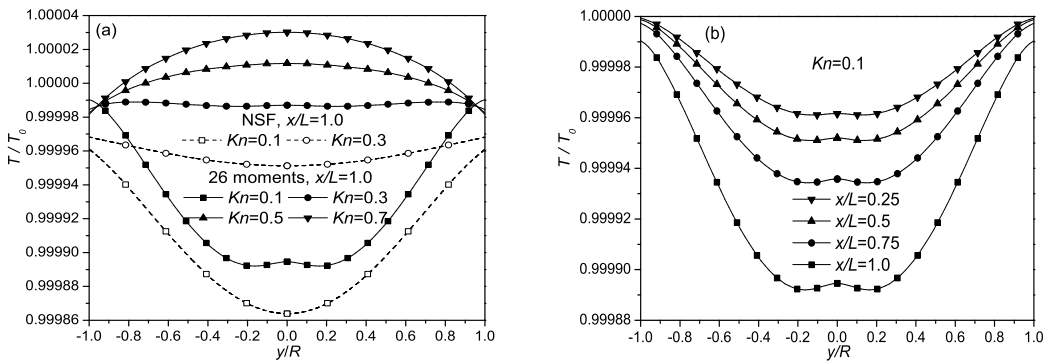


Figure 10: Distribution of the dimensionless temperature along the y -direction in the microtube. (a) At different Knudsen numbers. (b) At different streamwise positions.

velocity at different streamwise locations are shown in Fig. 9(b) at $Kn=0.5$. It is seen that the bimodal profile becomes more evident from the inlet to outlet.

Fig. 10 presents the temperature distribution along the y -direction. We can see that when the Knudsen number is smaller, the expansion cooling is dominant while the viscous heating effect becomes more and more dominant as the Knudsen number increases since the expansion cooling heat transfer effect reduces at larger Knudsen number. Compared to Fig. 6(a) for a parallel channel, we can see that the viscous heating effect for a circular tube is more evident at larger Knudsen number since the parallel channel is of stronger expansion cooling heat transfer character than the circular tube. Similar to the parallel channel, the expansion cooling effect increases from the inlet to outlet as shown in Fig. 10(b).

The spanwise velocity in the microtube normalized by u_{max} of the outlet is shown in Fig. 11 when $Kn=0.3$ and $P_i=2.0$. The numerical results of the 26 moment method in Fig. 11(a) show that there appears annular peak in the distribution of the spanwise velocity. In addition, the phenomenon of two peaks of spanwise velocity becomes more ob-

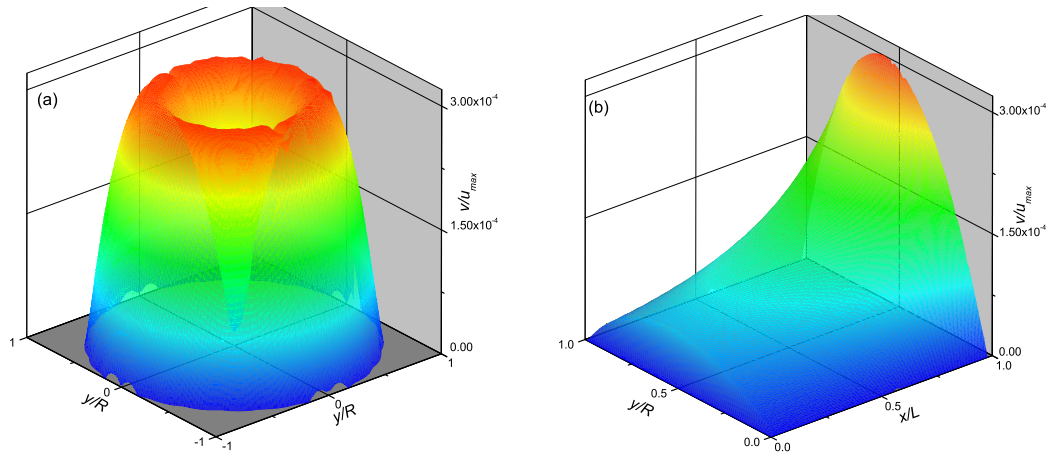


Figure 11: Spanwise velocity for pressure-driven flow through a long microtube with $Kn=0.3$ and $P_i=2.0$. (a) At outlet cross-section. (b) Along the streamwise direction.

vious along the streamwise direction as shown in Fig. 11(b). To the authors' best knowledge, it is for the first time to capture the unique bimodal profiles of streamwise and spanwise velocity and temperature through a long circular microtube. Further studies are expected to verify the interesting phenomena.

The friction coefficient in a long microtube is similar to that in a long microchannel, and the macroscopic expression with different slip velocity models is [32]

$$fRe = \frac{16}{1 + 8A_1Kn + 16A_2Kn^2}. \quad (4.4)$$

A_1 and A_2 are the coefficients of the slip velocity models. We can also derive [32]

$$fRe = \frac{\sqrt{\pi}}{KnQ}. \quad (4.5)$$

Here Q is the non-dimensional flow rate decided by the linearized Boltzmann solution for a circular microtube [35]. The effect of the Kn on fRe is shown in Fig. 12. Similar to the parallel channel, the present numerical results agree well with Eq. (4.5) by using the non-dimensional flow rate data from the linearized Boltzmann solution. The second-order Srekanth's model with $A_1 = 1.1466$ and $A_2 = 0.14$ is in rough agreement with the present numerical results, followed by the Mitsuya model. The first-order Maxwell slip model deviates the largest again.

5 Conclusions

In this paper, the 26 moment equations are employed to study non-equilibrium gas flow in the microfluidic constructions. The extended thermodynamic approach has been val-

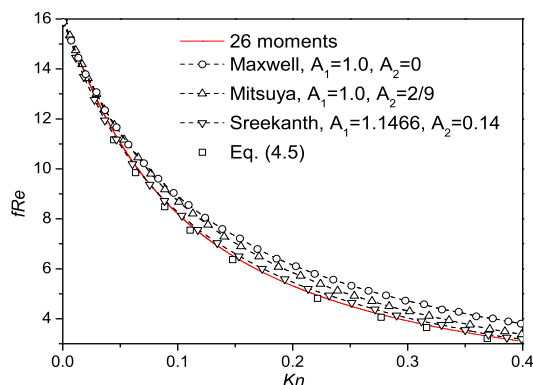


Figure 12: The Poiseuille number against the Knudsen number in a long microtube, compared with the linearized Boltzmann equation solution [35] and macroscopic equations with different slip velocity models [32].

idated by numerical simulations of heat transfer between two parallel plates with different temperatures and also gas flow characteristics in a long pressure-driven parallel microchannel and circular microtube with different outlet Knudsen numbers. The R26 method predicts better results in the microfluidic structures than the R13 method and the NSF with second-order boundary conditions, and the results agree well with available DSMC data. The predicted friction coefficients for pressure-driven parallel microchannel and circular microtube are also in good agreement with the analytical solution by using the flow rate of the linearized Boltzmann equation solution. In addition, the unique bimodal profiles along the radius for velocity and temperature in the pressure-driven circular microtube flow are captured. It is demonstrated that the 26 moment method can predict heat transfer and flow characteristics in non-equilibrium state in the early transition regime.

Acknowledgments

This work is supported by the National Natural Science Foundation of China under grant number 51076125, and the Science and Technology Research Development Program of Shaanxi Province under grant number 2010KJXX-01. Gu and Emerson would like to thank the Engineering and Physical Sciences Research Council (EPSRC) for their support of Collaborative Computational Project 12 (CCP12).

References

- [1] M. Gad-el-Hak. The Fluid mechanics of microdevices-the Freeman Scholar lecture. *ASME J. Fluids Eng.*, 121: 5-33, 1999.
- [2] A. Beskok. Validation of a new velocity-slip model for separated gas microflows, *Num. Heat Transfer, Part B*, 40: 451-471, 2001.

- [3] C. Cercignani. *The Boltzmann Equation and Its Applications*. Springer-Verlag, New York, 1988.
- [4] G. Bird. *Molecular Gas Dynamics and the Direct Simulation of Gas Flows*. Clarendon Press, Oxford, 1994.
- [5] G. H. Tang, W. Q. Tao and Y. L. He. Lattice Boltzmann method for gaseous microflows using kinetic theory boundary conditions. *Phys. Fluids*, 17: 058101, 2005.
- [6] G. H. Tang, Y. H. Zhang, X. J. Gu and D. R. Emerson. Lattice Boltzmann modelling Knudsen layer effect in non-equilibrium flows. *Europhys. Lett.*, 83: 40008, 2008.
- [7] L. Mieussens. Discrete-velocity models and numerical schemes for the Boltzmann-BGK equation in plane and axisymmetric geometries. *J. Comput. Phys.*, 162: 429-466, 2000.
- [8] F. Sharipov. Non-isothermal gas flow through rectangular microchannels. *J. Micromech. Microeng.*, 9: 394-401, 1999.
- [9] V. A. Titarev. Implicit unstructured-mesh method for calculating Poiseuille flows of rarefied gas. *Commun. Comput. Phys.*, 8: 427-444, 2010.
- [10] K. Xu and J. C. Huang. A unified gas-kinetic scheme for continuum and rarefied flows. *J. Comput. Phys.*, 229: 7747-7764, 2010.
- [11] X. J. Gu and D. R. Emerson. A high-order moment approach for capturing non-equilibrium phenomena in the transition regime. *J. Fluid Mech.*, 636: 177-216, 2009.
- [12] P. Taheri, M. Torrilhon and H. Struchtrup. Couette and Poiseuille microflows: Analytical solutions for regularised 13-moment equations. *Phys. Fluids*, 21: 017102, 2009.
- [13] X. J. Gu, D. R. Emerson and G. H. Tang. Kramers' problem and the Knudsen minimum: A theoretical analysis using a linearised 26-moment approach. *Contin. Mech. Thermodyn.*, 21: 345-360, 2009.
- [14] P. Taheri and H. Struchtrup. An extended macroscopic transport model for rarefied gas flows in long capillaries with circular cross section. *Phys. Fluids*, 22: 112004, 2010.
- [15] X. J. Gu and D. R. Emerson. Modeling oscillatory flows in the transition regime with a high-order moment method. *Microfluid. Nanofluid.*, 10: 389-401, 2011.
- [16] H. Grad. On the kinetic theory of rarefied gases. *Comm. Pure Appl. Math.*, 2: 331-407, 1949.
- [17] H. Struchtrup and M. Torrilhon. Regularization of Grad's 13 moment equations: Derivation and linear analysis. *Phys. Fluids*, 15: 2668-2680, 2003.
- [18] H. Struchtrup. *Macroscopic Transport Equations for Rarefied Gas Flows*. Springer, Berlin Heidelberg, 2005.
- [19] D. A. Lockerby, J. M. Reese and M. A. Gallis. The usefulness of higher-order constitutive relations for describing the Knudsen layer. *Phys. Fluids*, 17: 100609, 2005.
- [20] D. A. Lockerby and J. M. Reese. On the modelling of isothermal gas flows at the microscale. *J. Fluid Mech.*, 604: 235-261, 2008.
- [21] J. B. Young. Calculation of Knudsen layers and jump conditions using the linearized G13 and R13 moment methods. *Int. J. Heat Mass Transfer*, 54: 2902-2912, 2011.
- [22] H. Struchtrup and M. Torrilhon. Higher order effects in rarefied channel flows. *Phys. Rev. E*, 78: 046301, 2008
- [23] J. C. Maxwell. On stresses in rarefied gases arising from inequalities of temperature. *Phil. Trans. Roy. Soc.*, 17: 231-256, 1879.
- [24] H. Struchtrup and W. Weiss. Temperature jump and velocity slip in the moment method. *Contin. Mech. Thermodyn.*, 12: 1-18, 2000.
- [25] N. G. Hadjiconstantinou. Oscillatory shear-driven gas flows in the transition and free molecular flow regimes. *Phys. Fluids*, 17: 100611, 2005.
- [26] S. V. Patankar. *Numerical Heat Transfer and Fluid Flow*. Hemisphere Publishing Corpora-

- tion, 1980.
- [27] C. M. Rhie and W. L. Chow. Numerical study of turbulent flow past an airfoil with trailing edge separation. *AIAA J.*, 21: 1525-1532, 1983.
 - [28] M. A. Gallis, D. J. Rader and J. R. Torczynski. Calculations of the near-wall thermophoretic force in rarefied gas flow. *Phys. Fluids*, 14: 4290-4301, 2002.
 - [29] Q. Li, Y. L. He, G. H. Tang and W. Q. Tao. Lattice Boltzmann modeling of microchannel flows in the transition flow regime. *Microfluid. Nanofluid.*, 10: 607-618, 2011.
 - [30] C. Shen, D. B. Tian, C. Xie and J. Fan. Examination of the LBM in simulation of microchannel flow in transitional regime. *Microscale Thermal Eng.*, 8: 423-432, 2010.
 - [31] E. B. Arkilic, M. A. Schmidt and K. S. Breuer. Slip flow in microchannel. *J. Microelectromech. Syst.*, 6: 167-174, 1997.
 - [32] G. H. Tang, Y. L. He and W. Q. Tao. Comparison of gas slip models with solutions of linearized Boltzmann equation and direct simulation of Monte Carlo method. *Int. J. Mod. Phys. C*, 18: 203-216, 2007.
 - [33] N. G. Hadjiconstantinou and Simek O. Constant-wall-temperature Nusselt number in micro and nano-channels. *ASME J. Heat Transfer* 124(2): 356-364, 2002.
 - [34] T. Ohwada, Y. Sone and K. Aoki. Numerical analysis of the Poiseuille and thermal transpiration flows between two parallel plates on the basis of the Boltzmann equation for hard-sphere molecules. *Phys. Fluids A*, 1: 2042-2049, 1989.
 - [35] S. K. Loyalka and S. A. Hamoodi. Poiseuille flow of a rarefied gas in a cylindrical tube: Solution of linearized Boltzmann equation. *Phys. Fluids A*, 2: 2061-2065, 1990.